Human Molecular Genetics, 2017, Vol. 26, No. 15 2961–2974

doi: 10.1093/hmg/ddx186
Advance Access Publication Date: 9 May 2017
Original Article

ORIGINAL ARTICLE

Platinum-induced mitochondrial DNA mutations confer lower sensitivity to paclitaxel by impairing tubulin cytoskeletal organization

Giulia Girolimetti[1], Flora Guerra[2], Luisa Iommarini[3], Ivana Kurelac[1], Daniele Vergara[2], Michele Maffia[2], Michele Vidone[1], Laura Benedetta Amato[1], Giulia Leone[3], Sabrina Dusi[1], Valeria Tiranti[4], Anna Myriam Perrone[5], Cecilia Bucci[2], Anna Maria Porcelli[3,6,*] and Giuseppe Gasparre[1,*]

[1]Department of Medical and Surgical Sciences, Unit of Medical Genetics, University Hospital S.Orsola-Malpighi, 40138 Bologna, Italy, [2]Department of Biological and Environmental Sciences and Technologies, University of Salento, 73100 Lecce, Italy, [3]Department of Pharmacy and Biotechnology, University of Bologna, 40126 Bologna, Italy, [4]Unit of Molecular Neurogenetics, Pierfranco and Luisa Mariani Centre for the Study of Mitochondrial Disorders in Children, Foundation IRCCS Neurological Institute Carlo Besta, 20126 Milan, Italy, [5]Unit of Gynecologic Oncology, S.Orsola-Malpighi Hospital, 40138 Bologna, Italy and [6]Interdepartmental Center for Industrial Research, Health Sciences and Technologies (CIRI-HST), University of Bologna, 40126 Bologna, Italy

*To whom correspondence should be addressed at: Dept. of Pharmacy and Biotechnology - FABIT, University of Bologna, via Selmi 3, 40126 Bologna (BO), Italy. Tel. +39 051 2091282; Email: annamaria.porcelli@unibo.it (A.M.P.); Unit of Medical Genetics – DIMEC, University of Bologna, Via G. Massarenti 9, 40138 Bologna (BO), Italy. Tel: +39 051 2088430; Fax: +39 051 2088416; Email: giuseppe.gasparre@gmail.com (G.G.)

Abstract

Development of chemoresistance is a cogent clinical issue in oncology, whereby combination of anticancer drugs is usually preferred also to enhance efficacy. Paclitaxel (PTX), combined with carboplatin, represents the standard first-line chemotherapy for different types of cancers. We here depict a double-edge role of mitochondrial DNA (mtDNA) mutations induced in cancer cells after treatment with platinum. MtDNA mutations were positively selected by PTX, and they determined a decrease in the mitochondrial respiratory function, as well as in proliferative and tumorigenic potential, in terms of migratory and invasive capacity. Moreover, cells bearing mtDNA mutations lacked filamentous tubulin, the main target of PTX, and failed to reorient the Golgi body upon appropriate stimuli. We also show that the bioenergetic and cytoskeletal phenotype were transferred along with mtDNA mutations in transmitochondrial hybrids, and that this also conferred PTX resistance to recipient cells. Overall, our data show that platinum-induced deleterious mtDNA mutations confer resistance to PTX, and confirm what we previously reported in an ovarian cancer patient treated with carboplatin and PTX who developed a quiescent yet resistant tumor mass harboring mtDNA mutations.

Received: February 28, 2017. **Revised:** April 29, 2017. **Accepted:** May 5, 2017

Introduction

Onset of chemoresistance is a cogent issue in clinical oncology and a number of different human neoplasms are treated with more than one anticancer drug with the aim of preventing resistance. One of the most widely used combination of antineoplastic agents is formed by platinum-derived compounds such as Cisplatin (cis-Pt) and taxanes such as paclitaxel (PTX), which are administered in the case, among others, of Non-small Cell Lung cancer (NSCLC) (1), esophageal cancer (2) and ovarian cancer (OC) (3). Platinum compounds are inducers of DNA adducts that impede DNA replication and transcription, whereas PTX is a microtubules disassembly inhibitor. Cancer cells typically present high proliferation rates that render them more susceptible to these anticancer drugs compared to normal cells (4). Intrinsic and acquired resistance to chemotherapy is nonetheless the major obstacle for successful therapy. For instance, in the case of OC, initially nearly 75% patients respond favorably to combined chemotherapy, but subsequently a large number acquires resistance (3).

Previous studies revealed that cis-Pt can also accumulate in mitochondria inducing cis-Pt-mitochondrial DNA (mtDNA) adducts (5) that may damage mtDNA and generate mutations that may ultimately provide an energetic dysfunction contributing to metabolic remodeling (6). MtDNA mutations are frequently associated with virtually all types of cancer as somatic events (7) and changes in the metabolic status of cancer cells and in tumorigenic potential *in vivo* are closely related to the degree of respiratory chain defect, which in turn depends on the specific type of mtDNA mutation (8). Studies of energetic metabolism clearly indicate that cancer cells, which often prefer aerobic glycolytic metabolism, are able to shift from glycolysis to re-established oxidative metabolism during waves of cancer progression (9), suggesting that a certain degree of mitochondrial function and wild-type mtDNA must be maintained (8). Interestingly, disruptive mtDNA mutations are genetic hallmarks of oncocytic tumors, a class of neoplasms usually displaying a low-proliferating, non-invasive behavior (10), where they contribute to keeping cancer cells in a low-metabolism quiescent state through an *oncojanus* effect (11).

We previously reported the acquisition of an oncocytic phenotype in a residual OC mass after carboplatin/PTX chemotherapy (12), associated with occurrence of a respiratory complex I (CI) disruptive homoplasmic mutation in the *MT-ND4* gene occurring exclusively in the post-chemotherapy residual nodule. We hypothesized that this mutation might determine an energetic defect which may represent an advantage in the selection of a resistant tumor clone since PTX may be less effective on non-proliferative cells, suggesting a correlation between an inefficient mitochondrial oxidative metabolism and the acquisition of PTX resistance (12, 13).

In this study, we modeled what we previously observed to occur *in vivo* (12) starting from a cancer cell line of gynecologic origin (C13) treated with platinum, which shows accumulation of mtDNA mutations. We demonstrate that such platinum-induced mtDNA lesions imply a bioenergetic deficit that contributes to reduce cell proliferation and to hamper cytoskeletal organization, thus increasing PTX resistance as a drawback, tracing a causative link between occurrence of pathogenic mtDNA mutations and onset of chemoresistance upon cis-Pt/PTX combined therapy. We further show that such a bioenergetic and cytoskeletal phenotype is transferred along with the mtDNA mutations in cancer cells with a different nuclear background by the means of trans-mitochondrial hybrids (cybrids), where it confers PTX resistance.

Results

Platinum-induced mtDNA mutations confer resistance to PTX along with a lower replicative and tumorigenic potential and are positively selected by PTX treatment

With the aim to validate the hypothesis that platinum compounds may lead to accumulation of mtDNA mutations, we used the 2008 cell line and its syngenic cis-Pt resistant counterpart C13. Whole mtDNA sequencing of both cell lines confirmed exclusively in C13 the occurrence of two heteroplasmic mutations, namely the m.13828C > T in *MT-ND5* and the m.8156G > T in *MT-CO2*, subunits of respiratory CI and complex IV (CIV), respectively (Fig. 1A) (14). Lack of these mutations in 2008 cells was confirmed by the measurement of fine heteroplasmy using Denaturing High Performance Liquid Chromatography (DHPLC) (Supplementary Material, Fig. S1A). Both mutations imply an amino acid change, p.498Leu > Phe for the m.13828C > T and p.191Val > Leu for the m.8156G > T, and have a nucleotide variability value of zero according to HmtDB, indicating they were novel and possibly pathogenic. In order to understand whether the heteroplasmy was cell-based or rather population-based, i.e. whether each C13 cell has the same degree of heteroplasmy or two different C13 subpopulations coexist with different heteroplasmy levels, we dilution-cloned C13 and sequenced mtDNA obtained from re-expanded clonal populations. Most clones were still heteroplasmic as the parental C13, however several of them, renamed $C13^{hom}$ (Fig. 1A), harbored both mutations in homoplasmy. These findings suggested that both lesions co-occur on the same mtDNA molecule and that their homoplasmic status may cause an OXPHOS damage. Following our initial hypothesis, we focused from here onwards on C13 and $C13^{hom}$, and proceeded to test their sensitivity to PTX. Interestingly, $C13^{hom}$ displayed a significantly lower proliferation rate (Fig. 1B), which was concordant with a much higher PTX IC50 than C13 (3nM compared to 1 nM of C13 - Fig. 1C), and they appeared to be poorly affected by the same drug concentration that, instead, blunted colony formation of C13 in a clonogenic assay (Fig. 1D–E). Similarly, anchorage-independent growth of C13 only was hampered by PTX treatment (Fig. 1F–G). We were hence prompted to understand whether upon PTX treatment the C13 homoplasmic subpopulation would be positively selected. To this aim, we treated C13 cells with 3nM PTX for 7 days and picked the surviving cells. Re-sequencing of mtDNA revealed that the surviving C13 population was nearly homoplasmic for both mutations (Fig. 1H). Overall, these findings point to the achievement of a homoplasmic condition of mtDNA mutations as a strong selective advantage during PTX treatment. Further, the appearance of chromatin condensation and fragmentation found in C13 cells suggests that they are more prone than $C13^{hom}$ to undergo to an apoptotic type of cell death after PTX treatment (Fig. 1I). These results were confirmed by using an Annexin V (AV) and Propidium Iodide (PI) staining assay in flow cytometry (Fig. 1J). Indeed, a striking increase of AV/PI double positive cell population was observed only in C13 cells after 24 h of treatment with 3nM PTX (quadrant top right C13 treated cells), indicating the occurrence of late apoptotic events (Fig. 1J).

Resistance to PTX is transferred along with mtDNA mutations and with a slower oxidative metabolism, independently from ROS production

To ensure that the homoplasmy of the two mutations results in an actual functional impairment, the bioenergetic competence of $C13^{hom}$ and C13 cells was determined. Basal and FCCP

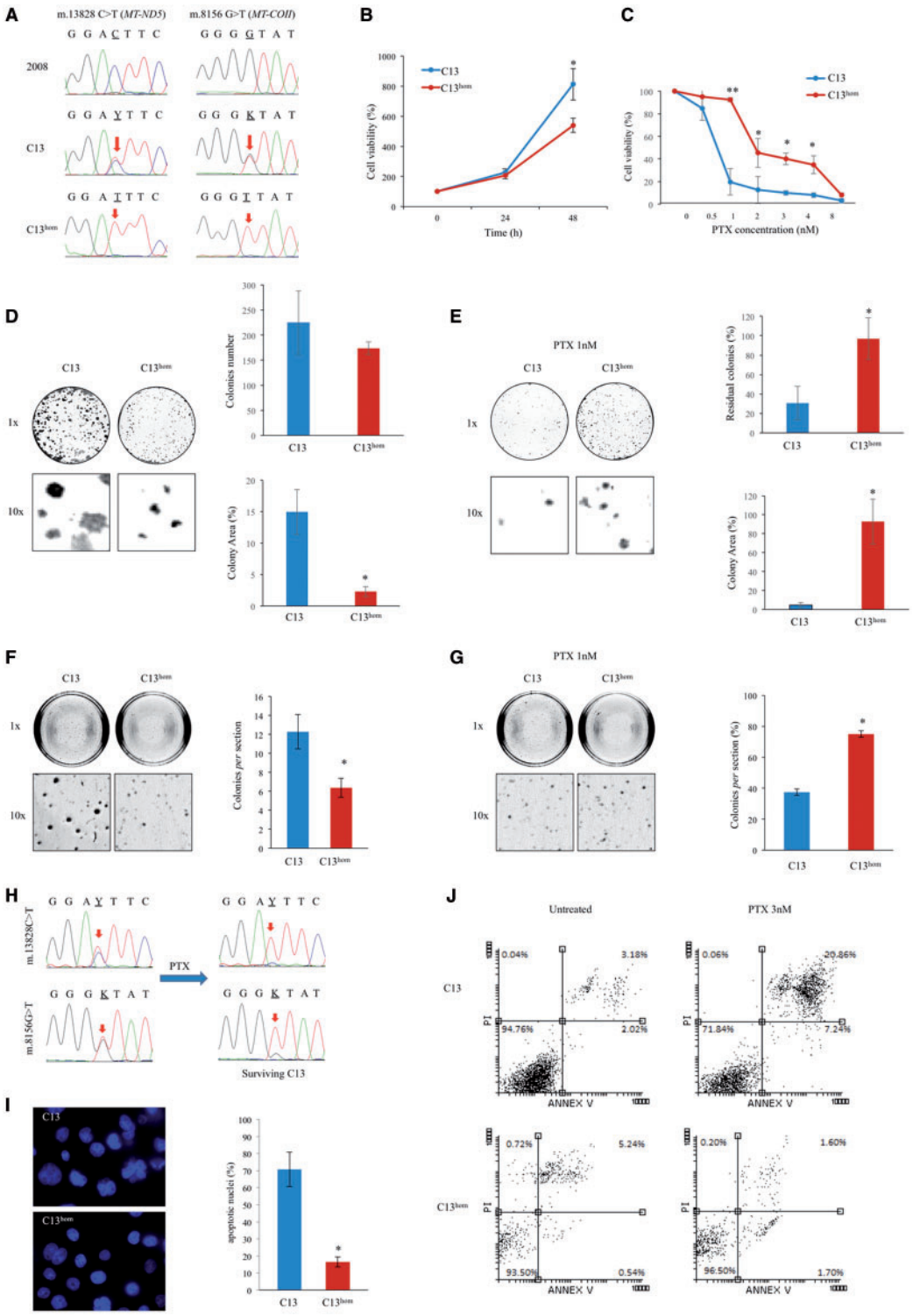

Figure 1. Pathogenic mtDNA mutations confer PTX resistance in a cancer cell line of gynecologic origin. (**A**) Electropherograms showing occurrence of the m.13828C > T and m.8156G > T mutations in cisplatin-resistant C13 cell. (**B**) Viability of heteroplasmic (C13) and homoplasmic (C13^{hom}) cancer cell lines in basal conditions. Data are presented as mean ± SE normalized to T0 ($n = 6$; *$P < 0.05$). (**C**) Viability of C13 and C13^{hom} cancer cell lines during 72 h treatment with increasing PTX concentrations. Data are presented as mean ± SD normalized to T0 ($n = 3$; *$P < 0.05$; **$P < 0.01$). (**D**) Capacity of C13 and C13^{hom} cells to form colonies analyzed in basal conditions. Data are presented as mean absolute value ± SD ($n = 3$; *$P < 0.05$). Magnifications 1× and 10× are shown. (**E**) Capacity of C13 and C13^{hom} to form colonies analyzed upon 1 nM PTX treatment. Data are presented as mean percentage of residual colonies normalized to untreated control ± SD ($n = 3$; *$P < 0.05$). Magnifications 1× and 10× are shown. (**F**) Capacity of C13 and C13^{hom} to grow in anchorage-independent manner in basal conditions. Data are presented as mean absolute value ± SD ($n = 3$; *$P < 0.05$). Magnifications 1× and 10× are shown. (**G**) Capacity of C13 and C13^{hom} to grow in anchorage-independent manner analyzed upon 1nM PTX treatment. Data are presented as mean percentage of residual colonies normalized to untreated control ± SD ($n = 3$; *$P < 0.05$). Magnifications 1× and 10× are shown. (**H**) Electropherograms of C13 cells showing selection of m.13828C > T and m.8156G > T mutations upon 7-day treatment with PTX (3nM). (**I**) Hoechst (10 μg/ml) staining of C13 and C13^{hom} nuclei upon 24-h PTX (3nM) treatment. Magnification 60×. Data show the mean percentage of apoptotic nuclei counted in 10 random areas ± SE ($n = 3$; *$P < 0.05$). (**J**) Evaluation of apoptosis upon treatment with 3nM PTX for 24 h in C13 and C13^{hom} cells using AV/PI staining in flow cytometry. Fluorescent signal of AV or PI in treated and untreated cells are shown in dot plots. The percentage of cells within each quadrant is indicated.

stimulated respiration, and spare respiratory capacity were significantly reduced in C13^{hom}, whereas their glycolytic function and the level of lactate was comparable between hetero- and homoplasmic cells (Fig. 2A–C), highlighting a bioenergetic deficit in C13^{hom} compared to C13 cells and a functional significance of the homoplasmic mtDNA mutations. To provide a proof of principle that such mitochondrial defect and lower sensitivity to PTX may be induced by the mtDNA from C13^{hom}, we generated and characterized a series of osteosarcoma 143B-derived cybrid clones from both C13 (HC13) and C13^{hom} cells (HC13^{hom}) (Supplementary Material, Fig. S1B). This approach allows excluding a possible nuclear contribution on the resistant phenotype that may have occurred after the C13 serial dilution and repopulation. Similarly to the parental cell lines, HC13^{hom} cells showed decreased oxygen consumption rate compared to HC13 (Fig. 2D). This finding was strengthened by the observation that the ATP synthesis driven by CI, complex II or III substrates was markedly decreased in HC13^{hom} cells, suggesting that the mutation in complex IV may likely act as a bottleneck point of the respiratory chain to affect ATP production, determining an overall defective bioenergetic phenotype in homoplasmic cybrids exclusively (Fig. 2E). Such energetic damage was indeed sufficient to nearly double PTX IC50 in HC13^{hom} cells compared to HC13 from 2.1 to 4nM (Fig. 2F), indicating that the resistant phenotype to PTX was exclusively to be attributed to mtDNA. Moreover, resistance was specific for PTX, since the IC50 for carboplatin, for instance, was not substantially different between homoplasmic and heteroplasmic cells (18.7 μM for C13^{hom} compared to 25.1 μM for C13 and 27 μM for HC13^{hom} compared to 33.9 μM for HC13).

In the search for a link between mitochondrial dysfunction, lower tumorigenic potential and PTX resistance, we next investigated whether a different reactive oxygen species (ROS) production may occur between heteroplasmic and homoplasmic cells, since ROS have been often called into play as promoters of tumorigenicity in cells carrying mtDNA lesions (15). The impairment of respiratory chain function of C13^{hom} cells was associated with a significant decrease of H_2O_2 production compared to C13 (Fig. 2G), suggesting that higher ROS levels may at least in part explain the higher tumorigenic potential of C13. We hence hypothesized that, this being the case, lowering ROS levels in C13 would decrease their proliferation as well as sensitivity to PTX. However, treatment with anti-oxidants ruled out a potential contribution of ROS in determining the sensitivity to PTX of C13^{hom} cells (Supplementary Material, Fig. S2).

MtDNA-mutated cells display a lower motility and migratory capacity associated with their slower metabolism

To delve into the mechanisms underlying PTX resistance associated with the respiratory dysfunction in homoplasmic cells, we performed non-hypothesis based, large-scale proteome and metabolome analyses on C13^{hom} and C13. The proteome pattern showed that two functional gene ontology (GO) categories were significantly altered between the two cell lines, the first being the *TCA cycle* (Fig. 3A, Tables 1 and 2). Mitochondrial fumarate hydratase (FUMH) and pyruvate carboxylase (PYC) were significantly decreased in C13^{hom} cells, suggesting a slower TCA cycle with an impaired anaplerosis, as PYC contributes to the replenishment of oxaloacetate. Concordantly, all TCA cycle metabolite levels were decreased in C13^{hom} cells as measured by a metabolome analysis (Fig. 4), with the exception of succinate. Interestingly, the enzyme that produces succinate, i.e. α-ketoglutarate (α-KG) dehydrogenase (ODO1) was the only enzyme of the TCA cycle which resulted to be significantly increased in the proteome analysis, suggesting that homoplasmic cells are probably forced to use glutaminolysis to produce α-KG and in turn re-establish succinate levels, as it has been shown in cells with deleterious mtDNA mutations (6). These data clearly support an overall impairment of mitochondrial oxidative metabolism in C13^{hom} cells, which determines a lower ability of these cells to perform a sustained replication activity. Interestingly, the other GO category that was found significantly changed in C13^{hom} cells was the *Regulation of actin cytoskeleton*, which suggested that C13^{hom} cells remodulate cytoskeletal proteins. In particular, in C13^{hom} vinculin (VINC), cofilin (COF1) and profilin (PROF1) were upregulated while ezrin (EZRI) and moesin (MOES) were downregulated (Table 2, Fig. 3B). Furthermore, other actin cytoskeleton regulators changed their expression in C13^{hom}. Indeed, Heat Shock Protein Beta-1 (HSB1) and Annexin2 (ANXA2) increased, while F-actin-capping protein subunit beta (CAPZB) decreased (Table 2). All these changes negatively affect cell migration, invasion and metastasis, although in different ways, as previously reported (16), and are consistent with a more quiescent and less invasive phenotype of C13^{hom}. Although actin cytoskeleton is not the target of PTX, it is known that microtubules, microfilaments and intermediate filaments communicate continuously and are linked together by cytolinkers (17). Thus, changes in tubulin cytoskeleton are likely to affect also other cytoskeletal elements. Also, considering the interactions between mitochondria and actin and the fact that actin dynamics can be regulated by mitochondria (18), mtDNA mutations selected by PXT may indeed affect actin cytoskeleton. Western blot analyses confirmed the proteomic results as well as the assumption that C13^{hom} cells attempt to achieve a quiescent, rather than an overt tumorigenic proliferative state. Cyclin D1 (*CCND1*) was indeed nearly absent in C13^{hom} compared to C13 cells (Fig. 3B), reinforcing the hypothesis that these cells have a much slower progression through the G1/S phase of the cell cycle. Moreover, phosphorylation of ERK was found markedly decreased, suggesting these cells to have a lower tumorigenic potential (Fig. 3B). The decreased expression of E- and N-cadherin in C13^{hom} cells (Fig. 3B) was further indicative of a lower invasive and metastatic potential compared with C13, in agreement with their lower migratory capacity as shown *in vitro* (Fig. 3C). Lower expression of N-cadherin has been previously reported to inhibit invasiveness in different types of tumors (19). Instead, low expression of E-cadherin is usually associated with increased malignancy and invasiveness, but, at variance, in a few types of cancer, high E-cadherin expression correlates with invasiveness (20).

Platinum-induced mtDNA mutations induce a derangement of tubulin fibers and an impairment of Golgi motility

Last, we reasoned that cells whose sensitivity to PTX was decreased may have a lower capacity of assembling and disassembling microtubules. We hence challenged homoplasmic and heteroplasmic cells to activate microtubular function by performing a wound healing assay during which we observed the reorganization of tubulin as well as the polarization of the Golgi body, which is known to focally reorient towards the migration trajectory. Interestingly, the morphology of tubulin fibers was different in heteroplasmic *versus* homoplasmic cells, regardless of the nuclear background.

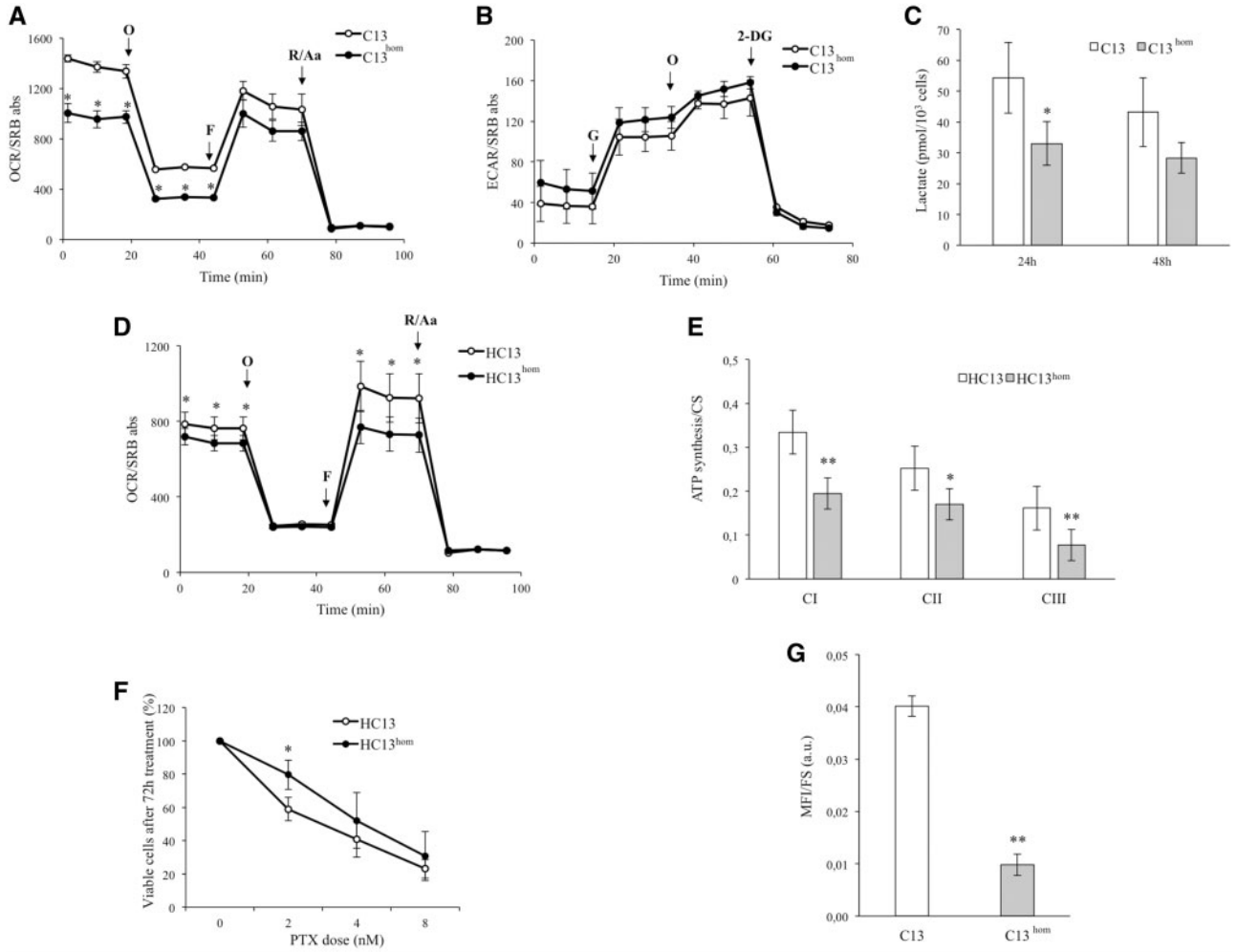

Figure 2. Cancer cells carrying pathogenic mtDNA mutations suffer bioenergetic deficit and display PTX resistance regardless of their nuclear background. (**A**) Oxygen consumption rate (OCR) measurements were performed in 10mM glucose medium upon injection of 1 μM oligomycin (O), 0.25 μM FCCP (F), 1 μM rotenone plus 1 μm antimycin A (R/Aa). Data (mean ± SE) are expressed as OCR (picomoles of O_2 per minute) normalized on SRB absorbance ($n = 3$; $^*P < 0.05$). (**B**) Extracellular acidification rate (ECAR) measurements performed in a medium devoid of glucose upon injection of 10mM Glucose (G), 1 μM oligomycin (O), 10mM 2-deoxyglucose (2-DG). Data (mean ± SE) are expressed as ECAR (mpH per minute) normalized on SRB absorbance ($n = 3$; $^*P < 0.05$). (**C**) L-lactate production of cells incubated in the presence of high glucose for 24 h and 48 h. Data (mean ± SE) are expressed as picomoles of L-lactate normalized on cell number ($n = 3$; $^*P < 0.05$). (**D**) Oxygen consumption rate (OCR) measurements in osteosarcoma cybrids, performed in 25mM glucose medium upon injection of 1 μM oligomycin (O), 0.25 μM FCCP (F), 1 μM rotenone plus 1 μm antimycin A (R/Aa). Data (mean ± SE) are expressed as OCR (picomoles of O_2 per minute) normalized on SRB absorbance ($n = 3$; $^*P < 0.05$). (**E**) Rate of mitochondrial ATP synthesis in digitonin-permeabilized osteosarcoma cybrid cells driven by pyruvate/malate (CI), succinate plus rotenone (CII) and reduced decylubiquinone (CIII). Data normalized for CS activity and protein content are mean ± SD ($n = 4$; $^*P < 0.05$; $^{**}P < 0.001$). (**F**) Viability of osteosarcoma cybrids during 72 h treatment with increasing PTX concentrations. Data are presented as mean ± SD normalized to T0 ($n = 3$; $^*P < 0.05$). (**G**) H_2O_2 production determined by flow cytometry using 2μm 2,7-dichlorodihydrofluorescein diacetate (H_2DCFDA) fluorescent dye. Data (mean ± SD) are expressed as mean fluorescence intensity (MFI) normalized on forward scatter (FS) as an indicator of cell size ($n = 3$; $^*P < 0.05$).

Indeed, C13 and HC13 displayed a canonical filamentous tubulin network (Fig. 3D, panels a and c and relative zoomed areas a.1 and c.1), whereas their homoplasmic counterparts showed a dotted pattern, with filamentous microtubules being nearly absent (Fig. 3D, panels b and d and relative zoomed areas b.1 and d.1). These differences were more pronounced in the two cybrids HC13 and HC13^{hom} (Fig. 3D, panels c-d) than in C13 and C13^{hom} (Fig. 3D, panels a-b), probably because of the C13 heterogeneous composition in terms of coexistence of homo/heteroplasmic-mutated subpopulations.

To test whether the tubulin asset was functional in driving organelle movement, we performed also immunofluorescence analysis using antibodies against giantin, an integral component of the Golgi membrane in order to highlight the Golgi body. We also used fluorescent phalloidin, a drug tightly and selectively binding to filamentous actin in order to observe cell morphology and DAPI to stain nuclei. Giantin labeling revealed that C13 and C13^{hom} are characterized by a fragmented Golgi (Fig. 3E, panel a-b) while cybrids show a canonical Golgi staining of large perinuclear structures (Fig. 3E panel c-d). To monitor reorientation of the Golgi, 6 h after the induction of cell migration by scratching the cell monolayer, we scored the cells facing the wound. C13 cells promptly reoriented all small Golgi fragments labeled by giantin towards the leading edge of migration (Fig. 3E, panel a). By contrast, most of C13^{hom} facing the wound presented the Golgi fragments distributed all around the nucleus without polarization (Fig. 3E, panel b). HC13 cells facing the wound, like C13, were able to reorient the Golgi apparatus

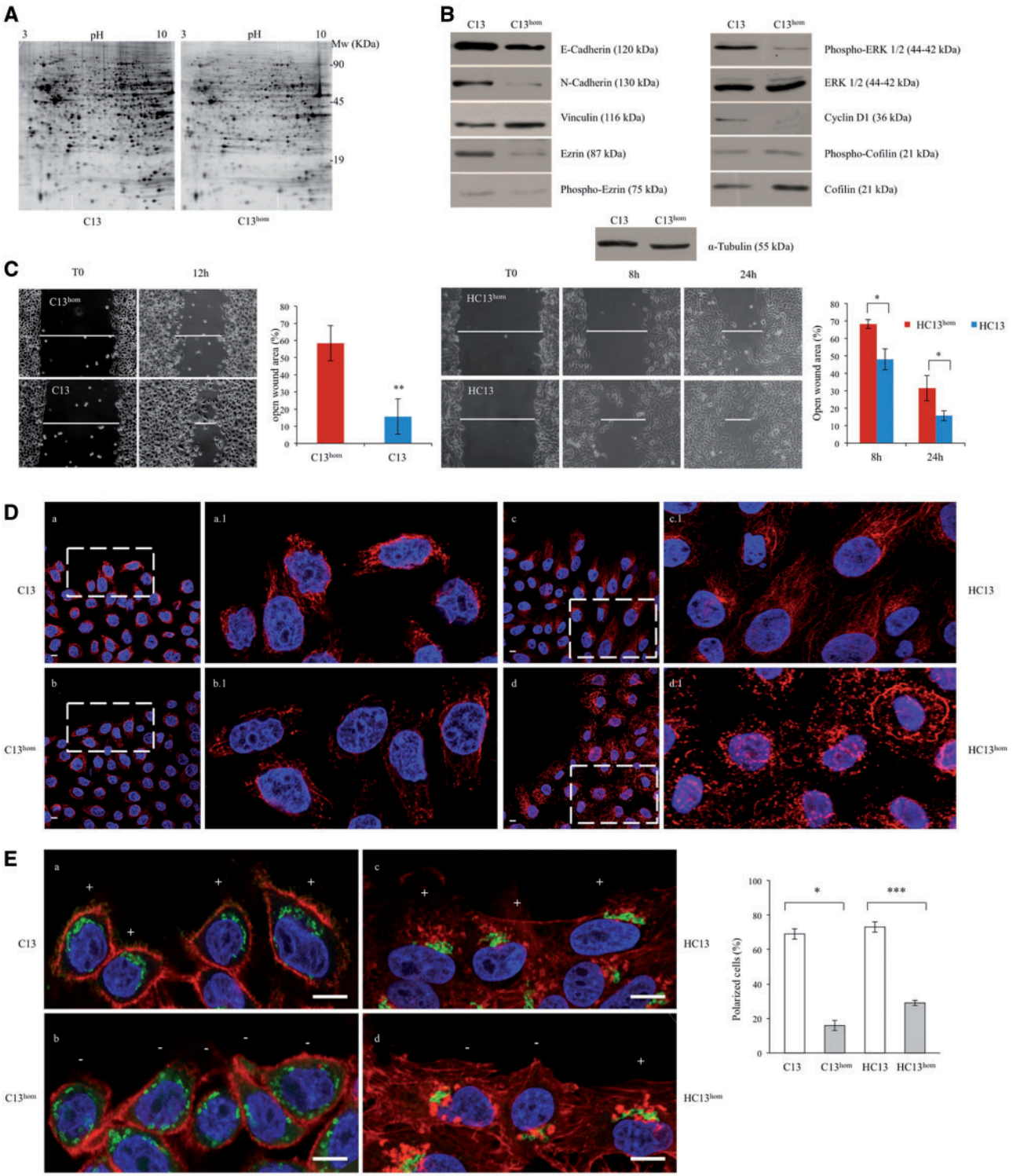

Figure 3. Homoplasmic cells show impairment in motility and cytoskeletal organization in association with their decreased tumorigenic potential and PTX resistance. (**A**) Representative 2-DE gel map of C13 and C13^{hom} cell proteins. A total of 80 μg of proteins were separated by 2-DE using a 13cm IPG strippH3–10NL and 12% SDS-PAGE. Proteins were visualized by silver staining. (**B**) Western Blot analysis of C13 and C13^{hom} cells showing expression levels of several of the proteins revealed as differentially expressed by the proteomics analyses as well as the expression levels of some cancer proliferation proteins are shown. A representative experiment of three is shown. (**C**) Wound healing assay in OC cells and cybrids. Cells were grown to nearly 90% confluence in 6-well plates. Data are presented as mean ± SD normalized to T0 ($n = 3$; $^{**}P < 0.01$). (**D**) Wound healing assay in C13 (panels a and a.1) and C13^{hom} (panels b and b.1) and their derived cybrids HC13 (panels c and c.1) and HC13^{hom} (panels d and d.1) seeded in round coverslips and subsequently stained with anti-tubulin antibody. Panels a, b, c and d correspond to images captured with Plan - Apochromat 63×/1.40na oil-immersion objective and dashed boxes represent zoomed areas (panels a.1, b.1, c.1 and d.1). Overlay of blue (λ_{ex}: 405nm; λ_{em}: 415–500nm) and red (λ_{ex}: 555nm; λ_{em}: 560–615nm) channels are shown. Nuclei (blue); Tubulin (red). Scale bars: 10 μm. (**E**) Giantin, phalloidin and DAPI staining of C13 and C13^{hom} (panels a and b) and their derived cybrids HC13 and HC13^{hom} (panels c and d) facing the wound. Plus (+) and minus (-) were used to indicate polarized and not polarized Golgi, respectively. Images were captured with Plan - Apochromat 63×/1.40na oil-immersion objective. Scale bars: 10 μm. Overlay images of blue, green and red (λ_{ex}: 555nm; λ_{em}: 560–615nm) channels are shown. Nuclei (blue); giantin (green); phalloidin (red). For quantification of Golgi reorientation only cells facing the wound were scored. Data are presented as mean ± SE ($^{*}P < 0.05$, $^{***}P < 0.001$).

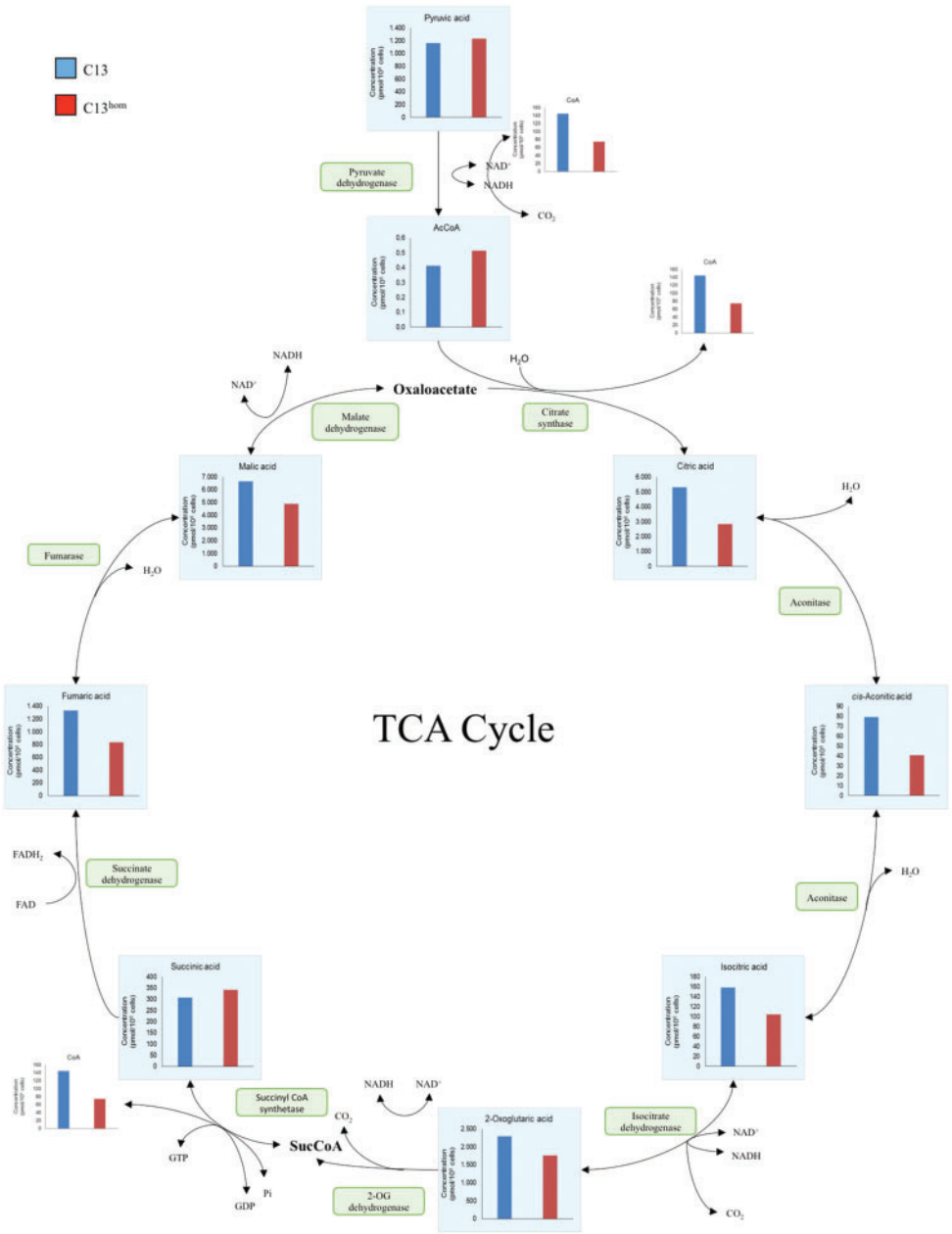

Figure 4. TCA cycle profile in C13 and C13^{hom}. The abundance of TCA metabolites was determined by metabolome analysis as described in Materials and Methods. The concentration of each TCA metabolite is expressed as picomoles per 1×10^6 cells. A representative experiment of two is shown.

towards the leading edge 6 h after the wound (Fig. 3E, panel c) while only few HC13^{hom} cells displayed a polarized distribution (Fig. 3E, panel d)

Overall, these data suggested that mtDNA mutations in homoplasmy were uniquely responsible for an impaired microtubular phenotype, with homoplasmic cells being less able to migrate due to a cytoskeleton impairment.

Discussion

In this paper, we show that mtDNA mutations that impinge on the metabolic features of cancer cells, occurring after treatment with platinum compounds, are able to confer resistance to PTX, as they induce the inability to trigger the intracellular modifications needed to migrate and invade. Our study stems from an *in vivo* observation of an OC patient who had developed a quiescent yet resistant mass after being treated with PTX and carboplatin, in which a somatic mtDNA deleterious mutation had accumulated to near-homoplasmy (12).

Both platinum-derived compounds and PTX are the preferential combinatorial treatment for several types of human neoplasms, and particularly are in the first line for OC, recently in further association with bevacizumab (21). It is however neglected that platinum acts to modify mtDNA as well as nuclear DNA, and it is likely that such damage persists as mtDNA is less prone to be efficiently repaired. Very few studies report the consequences of the use of platinum on the occurrence of mtDNA mutations (22), while they do not correlate the latter to

Table 1. Differentially expressed proteins identified by 2-DE and mass spectrometry analysis. Protein expression was determined by proteomic analysis as described in Materials and Methods. Proteins are listed using the accession number in Swiss-Prot/UniprotKB (www.uniprot.org/). Fold change ($C13^{hom}$/C13) was calculated dividing the average of %V of $C13^{hom}$ by the average of %V of C13 (%V = V single spot/V total spots included in the gel) using the Image Master 2D Platinum v5.0 software. T-test was performed by GraphPad v4.0 software to determine if the relative change was statistically significant ($P < 0.05$); *$P < 0.05$; **$P < 0.01$; ***$P < 0.001$. Abbreviation - MT/T: MALDI TOF/TOF

Swiss Prot accession no.	Protein name	Gene name	Fold change $C13^{hom}$/C13	*P*-value	Instrument
P47756	F-actin-capping protein subunit beta (CAPZB)	*CAPZB*	−1.5	**	**MT/T**
P04792	Heat shock protein beta-1 (HSPB1)	***HSPB1***	2.4	***	**MT/T**
P63244	Guanine nucleotide-binding protein subunit beta-2-like 1 (GBLP)	*GNB2L1*	−1.9	***	**MT/T**
Q16891	MICOS complex subunit MIC60 (MIC60)	*IMMT*	1.7	**	**MT/T**
P33993	DNA replication licensing factor MCM7 (MCM7)	*MCM7*	−1.6	**	**MT/T**
Q8WUM4	Programmed cell death 6 interacting protein (PDC6I)	***PDCD6IP***	1.7	**	**MT/T**
O00299	Chloride intracellular channel protein 1 (CLIC1)	*CLIC1*	−2.2	***	**MT/T**
P14866	Heterogeneus nuclear ribonucleoprotein L (HNRNPL)	*HNRNPL*	−1.5	**	**MT/T**
P50395	Rab GDP dissociation inhibitor beta (GDIB)	***GDI2***	1.5	**	**MT/T**
P23528	Cofilin (COF1)	*CFL1*	1.8	**	**MT/T**
P11586	C-1-tetrahydrofolate synthase, cytoplasmic (C1TC)	*MTHFD1*	1.6	**	**MT/T**
P15311	Ezrin (EZRI)	*EZR*	−2.4	***	**MT/T**
P26038	Moesin (MOES)	***MSN***	−1.6	**	**MT/T**
P11498	Pyruvate carboxylase, mitochondrial (PYC)	*PC*	−1.5	**	**MT/T**
P32119	Peroxiredoxin-2 (PRDX2)	*PRDX2*	1.8	**	**MT/T**
P07737	Profilin-1 (PROF1)	***PFN1***	2	***	**Esi-Trap**
P07355	Annexin A2 (ANXA2)	*ANXA2*	3.2	***	**MT/T**
P29401	Transketolase (TKT)	*TKT*	−1.6	**	**MT/T**
P34897	Serine hydroxymethyltransferase, mitochondrial (GLYM)	*SHMT2*	−2.1	***	**MT/T**
P35232	Prohibitin (PHB)	*PHB*	1.7	**	**MT/T**
Q02218	2-oxoglurate dehydrogenase, mitochondrial (ODO1)	*OGDH*	1.5	*	**MT/T**
P18206	Vinculin (VINC)	*VCL*	1.7	**	**Esi-Trap**
P06733	Alpha enolase (ENOA)	*ENO1*	−1.7	**	**MT/T**
Q8WVY7	Ubiquitin-like domain-containing CTD phosphatase 1 (UBCP1)	*UBLCP1*	−1.9	***	**MT/T**
Q15365	Poly(rC)-binding protein 1 (PCBP1)	*PCBP1*	−1.8	***	**MT/T**
P30153	Serine/threonine-protein phosphatase 2A 65 KDa regulatory subunit A alpha isoform (2AAA)	*PPP2R1A*	1.6	*	**MT/T**
P15531	Nucleoside diphosphate kinase A (NDKA)	***NME1***	1.7	**	**MT/T**
P04792	Heat shock protein beta-1 (HSPB1)	***HSPB1***	2	***	**MT/T**
Q99497	Protein DJ-1 (PARK7)	*PARK7*	1.5	*	**MT/T**
P62333	26S protease regulatory subunit 10B (PRS10)	*PSMC6*	1.6	*	**MT/T**
P49591	Serine–tRNA ligase, cytoplasmic (SYSC)	*SARS*	3.1	***	**MT/T**
P22234	Multifunctional protein ADE2 (PUR6)	*PAICS*	−1.7	**	**MT/T**
Q16531	DNA damage-binding protein 1 (DDB1)	*DDB1*	1.6	**	**MT/T**
P07954	Fumarate hydratase, mitochondrial (FUMH)	*FH*	−1.5	*	**MT/T**
P49915	GMP synthase (GUAA)	*GMPS*	−1.6	*	**MT/T**
P09960	Leukotriene A-4 hydrolase (LKHA4)	*LTA4H*	1.5	*	**MT/T**
P17931	Galectin-3 (LEG3)	***LGALS3***	1.9	***	**MT/T**

resistance to other drugs. Although it has been reported that mtDNA mutations may predispose to a chemoresistant phenotype, likely through causing a diminished capacity of undergoing mitochondria-dependent apoptosis (23), it is often neglected in these studies that accumulation of mtDNA lesions has invariably an impact on the cancer cell metabolic reprogramming (24). Notably, the type of mtDNA mutation is a pivotal feature in determining a cell fate (8). In this context, it is plausible that a severe mutation that decreases or does not alter promitogenic ROS production be favorably selected during a chemotherapic course aimed at targeting actively dividing cancer cells. Indeed, by causing a metabolic slowdown, highly deleterious mtDNA mutations act with *oncojanus* features (11), rendering cells quiescent/dormant (25) and therefore more resistant to agents such as PTX. Interestingly, overall, the combinatorial therapy, or at least platinum, may act like a selective pressure on cancer cells, favoring cells with a higher burden of mtDNA mutations and a slower metabolism. Such features, which are typical of dormant cancer cells, associate with a decrease, yet likely transient, in tumorigenic potential (25). Most interestingly, homoplasmic mtDNA lesions were sufficient to induce a significantly lower ability to rearrange the intracellular components to foster migration, which is essentially based on cytoskeletal remodeling. These data are supported by previous findings indicating a close link between different cytoskeletal elements and mitochondrial biogenesis and demonstrating the existence of a regulation mediated by mitochondria of the actin cytoskeleton (18). Tubulin, the main target of PTX, was profoundly affected in the presence

Table 2. TCA cycle and Regulation of Actin Cytoskeleton are the altered functional gene ontology (GO) categories between homo- and heteroplasmic cell lines. Protein dataset was subjected to KEGG pathway enrichment analysis using the software DAVID (david.abcc.ncifcrf.gov). Three proteins/genes of our list were included in the TCA cycle GO category ($P = 1.7 \times 10^{-2}$) and five were included in the Regulation of Actin Cytoskeleton GO category ($P = 9.1 \times 10^{-3}$). Proteins are listed using the accession number in Swiss-Prot/UniprotKB (www.uniprot.org/)

Pathway	Count	Involved genes	p-value	Benjamini
Regulation of actin cytoskeleton	5	• P23528 • P15311 • P26038 • P07737 • P18206	9.1e-3	3.1e-1
Citrate cycle (TCA cycle)	3	• P07954 • Q02218 • P11498	1.7e-2	3.0e-1

of homoplasmic mtDNA mutations, and although the direct mechanistic link was not the focus of this paper, the most plausible hypothesis is that a decreased energy capacity of these cells may slow down the highly energetic processes at the basis of cancer cell migration. It is not surprising that, therefore, these cells should respond less to PTX, as they dwell in a quiescent state that may likely be subsequently reactivated when therapy is released and mtDNA mutations shift back towards wild-type. In this frame, such subclones would be responsible for relapses at a later stage. To further support this picture is the notion that, unlike for nuclear genes, mtDNA mutations more easily revert, as pure homoplasmy is rather a virtual condition, and the shift towards the mutated or the wild-type variant through selective replication of the corresponding mtDNA molecules may be determined by a myriad of factors (7).

With respect to our previous *in vivo* study (12), it is worth mentioning that after over two years, the OC patient we thereby presented displayed relapses. It will be interesting to investigate whether subclones free of the mtDNA mutation have generated the secondarisms we observe. Interestingly, the residual mass had also acquired oncocytic features, a phenotype mainly associated to a low proliferative and low aggressive behavior, whose univocal genetic hallmark are deleterious mtDNA mutations (11). Oncocytic tumors have been often considered somewhat ambiguous entities due to their quiescent, yet chemoresistant phenotype, such as for instance in the thyroid, where they are suggestive of a poor prognosis on the basis of such resistance (10). In this paper we have attempted to link the occurrence of mtDNA mutations to the effects that a decreased metabolic activity has on the cells' ability to proliferate, migrate and invade, all hallmarks of aggressive cancers. The decrease of such potential, like in oncocytic tumors, has as a drawback an increased resistance to specific anti-cancer drugs.

In conclusion, we depicted a novel mechanism of chemoresistance and suggested that caution is warranted in the use of combinatorial therapies. An efficient therapy should also target metabolically less active dormant cells that have acquired mtDNA mutations, which survive through compensatory mitochondrial biogenesis, as in oncocytomas (10). Hence, a potential way to circumvent the acquisition of a resistant phenotype when mtDNA mutations are the main determinants may stand in the use of inhibitors of mitochondrial biogenesis, as it has already been suggested for relapsing melanomas (26). In such cases, blocking this biological process may prove to be lethal for quiescent subclones and prevent relapses. While these strategies become increasingly suggested to treat human neoplasms, mtDNA genotyping ought to be exploited to help predicting the response to pharmacological treatments in diagnostic procedures, particularly in light of the widespread use of deep sequencing technologies, which render whole mtDNA sequencing quick and inexpensive.

Materials and Methods

Human cancer cell lines

Human cell line 2008 of gynecologic origin and its cis-Pt-resistant subline C13 generated by growth in 1μM cis-Pt for 13 months were a kind gift of Dr. G. Marverti (University of Modena and Reggio Emilia, Italy) (14). The $C13^{hom}$ subline was obtained by dilution cloning. 2008, C13 and $C13^{hom}$ cell lines were grown in RPMI 1640 medium, supplemented with 10% FBS (Fetal Bovine Serum), L-glutamine (2mmol/L), penicillin (100 units/ml) and streptomycin (100 μg/ml), in a humidified incubator at 37 °C with 5% CO_2. The 2008 and C13 cell lines were used and mtDNA-genotyped in Catanzaro et al (14). We here reported the same mtDNA genotype after mtDNA resequencing, which served as an authentication for these cell lines. The mutation load of both C13 and $C13^{hom}$ cells was checked at every experiment by collecting aliquots and extracting total DNA. Heteroplasmy evaluation was performed each time by Sanger sequencing and, whenever necessary, by DHPLC as described.

Transmitochondrial cell hybrids (cybrids) generation

Cybrids were generated following a previously described protocol (27). Cybrids carried 143B.TK- osteosarcoma nucleus and C13 and $C13^{hom}$ mitochondria. Homoplasmic and heteroplasmic versions, here referred to as HC13 and $HC13^{hom}$, respectively, were grown in DMEM (Dulbecco's Modified Eagle Medium), supplemented with 10% FBS, L-glutamine (2 mmol/L), penicillin (100units/ml), streptomycin (100 μg/ml) and uridine (50 μg/ml) in a humidified incubator at 37 °C with 5% CO_2. To authenticate cybrid cell lines, the occurrence of the known *TP53* mutation g.13055G > C harbored by the parental 143B.TK- cells was verified by PCR and Sanger sequencing (11). Coexistence of the *TP53* mutation along with the two mtDNA mutations of C13 unequivocally identified cybrids.

Nucleic acid extraction and whole mtDNA amplification, sequencing and mutation screening

Whole genomic DNA was extracted using Mammalian Genomic DNA Miniprep Kit (Sigma-Aldrich, #G1N350) according to the manufacturer's protocols. Sanger sequencing of the entire mtDNA was performed following a quality-check protocol as

previously described (28). Mitochondrial DNA mutations were confirmed using a second PCR reaction. FASTA files were used as input for MToolBox (29) in order to annotate mitochondrial variants and related features, which read mapping, post-mapping processing, genome assembly, haplogroup prediction and variant annotation. Amino acid variability is also considered if the variant site is codogenic (30). Nucleotide site-specific variability was estimated on the multi-alignment of the updated healthy genomes reported in HmtDB (31).

Denaturing high performance liquid chromatography (DHPLC)

Following PCR amplification, samples were analyzed by WAVE Nucleic Acid Fragment Analysis System (Transgenomic). Primers used for the m.8156G > T/*MT-COII* mutation were: FW-5'-CGACTCCTTGACGTTGACAA-3' and RV-5'- GCTTTACAGGGGC TCTAGAG -3. Primers used for the m.13828C > T/*MT-ND5* mutation were: FW-5'- CGCTTCCCCACCCTTACTAA -3' and RV-5'-CGGTGTGTGATGCTAGGGTA -3'. Temperature optimization and sample analysis were performed by Navigator Software version 2.0. (Transgenomic). The standard and unknown samples were analyzed in the same running assay as previously described (32).

Cell viability measurements

Cell viability for HC13/HC13^{hom} was measured by the Sulforhodamine B (SRB) assay (Sigma-Aldrich, #S1402). SRB was used for cell density determination, based on the measurement of cellular protein content, as previously detailed (8). Cell viability for C13/C13^{hom} was measured by Trypan Blue (Sigma-Aldrich #T8154). After the staining with Trypan Blue, cells were counted with an optical microscope using a Neubauer hemocytometer. Cells were seeded in 24-well plates (1×10^4 cells/well) in complete medium, after 24 h cells were washed twice in PBS and incubated in different media. To evaluate cytotoxicity different concentrations of PTX (StressMarq, Bioscience Inc., #SIH-239) and carboplatin (Hospira) were used, depending on the nuclear background of cell lines. Cell viability was measured after 24, 48 and 72 h. IC50 was calculated after 72 h as the concentration that results in a 50% decrease in the number of cells compared to that of the untreated control.

Anchorage-independent colony formation assay

Anchorage-independent cell growth was determined for C13/C13^{hom} in 0.33% agarose with a 0.5% agarose underlay. Cell suspensions (2×10^4 cells per 32-mm dish) were plated in duplicate in semisolid medium (growth medium 10% FBS plus agar 0.33%) in absence or presence of PTX (1nM) and incubated at 37 °C in a humidified 5% CO_2 atmosphere (33). Colonies were counted after 10 days at a magnification of 10× with an inverted microscope (Nikon Diaphot, Nikon Instruments). Plate pictures and magnifications were obtained with Gel Logic 1500 molecular imaging apparatus (Kodak, Rochester). The percentage of residual colonies after PTX treatment was calculated as the number of colonies normalized to untreated controls for each cell line.

Clonogenic assay

Anchorage-dependent cell growth was determined for C13/C13^{hom}. Cell suspensions (500 cells per 32-mm dish) were plated in duplicate in absence or presence of PTX (1nM) and incubated at 37 °C in a humidified 5% CO_2 atmosphere. Colonies were fixed, stained, and analyzed after 7 days.

Clonogenic assay with antioxidants

The effect of antioxidants on colony formation was evaluated by treating cells with glutathione (GSH - 10mM; Sigma-Aldrich, #G6529), ascorbic acid (100μM; Merk Millipore, #100468) and TROLOX (1mM; Sigma-Aldrich, #238813) alone or in combination with 1nM PTX. Colonies were fixed, stained, and analyzed after 7 and 14 days (for C13 and C13^{hom} respectively), to allow C13^{hom} colonies to reach the same size as C13 and allow adequate comparison.

Apoptotic cell death determination

Nuclear DNA of C13 and C13^{hom} cells treated for 24 h with PTX (3nM) was visualized by staining for 30' at 37 °C with 5 μg/ml Hoechst 33342 (LifeTechnologies, #H3570). Fluorescence was visualized with a digital imaging system using an inverted epi-fluorescence microscope with 63X/1.4 oil objective (Diaphot, Nikon, Japan) and Omega Filter pinkel Set XF66-1 triband (Omega Optical Inc., Brattleboro,VT, USA). Images were captured with a back-illuminated Photometrics Cascade CCD camera system (Roper Scientific, Tucson, AZ, USA) and Metamorph acquisition/analysis software (Universal Imaging Corp., Downingtown, PA, USA). The fraction of apoptotic nuclei was determined in 10 different at 60× magnification fields for each sample. Phosphatidyl serine and cell permeabilization were determined by using Annexin V-FITC Apoptosis Kit (Novus Biologicals #NBP2-29373) following the manufacturer's protocol. Briefly, C13 and C13^{hom} cells were incubated with 3nM PTX for 24 h in complete medium, and untreated cells were used as controls. After 24 h, cells were harvested and counted, resuspended at the concentration of 1×10^6 cells/ml and washed twice in ice cold PBS. Aliquots of 100μL of cell suspension were stained for 20′ at room temperature and then samples were analyzed at flow cytometer Coulter Epics XL-MCL (Beckman Coulter) equipped with an argon ion laser at $\lambda = 488$nm and $\lambda = 620$nm; 5000 events were analyzed. Data were analyzed with WinMDI ver. 2.9 software (http://facs.scripps.edu/software.html; date last accessed April 2017).

Oxygen consumption rate (OCR) and extracellular acidification rate (ECAR)

OCR and ECAR were measured using the Seahorse XFe24 Extracellular Flux Analyzer (Seahorse Bioscience) as previously described (33). Mitochondrial respiration was evaluated using the Seahorse XF Cell Mito Stress Test Kit (Seahorse Bioscience, #103015-100), whereas glycolysis was determined by the Seahorse XF Glycolysis Stress Test Kit (Seahorse Bioscience, #103020-100) following the manufacturer's instructions. Cells were seeded (3×10^4 cells/well) into XFe24 cell culture plate and allowed to attach for 24 h. Three measurements of OCR/ECAR were obtained following injection of each drug and drug concentrations optimized on cell lines prior to experiments. At the end of each experiment, the medium was removed and SRB assay was performed to determine the amount of total cell proteins as described above. OCR and ECAR data were normalized to total protein levels (SRB protein assay, Sigma-Aldrich, #S1402) in each well. Each cell line was represented in 5 wells per experiment ($n = 3$ replicate experiments). Data are expressed as pmoles of O_2 per minute (OCR) or mpH per minute (ECAR) normalized on SRB absorbance.

Lactate production

Lactate concentration was determined by measuring NADH ($\lambda = 340$ nm; $\epsilon = 6.22\ mM^{-1}\ cm^{-1}$) production in a buffer containing 320mM glycine, 320 mM hydrazine, 2.4 mM NAD^+ and 2U/ml L-lactic dehydrogenase (LDH, Sigma-Aldrich, #L1006) as previously described (8). Data are expressed as pmoles of lactate produced by 1000 cells.

ATP synthesis assay

The rate of mitochondrial ATP synthesis driven by CI, CII and CIII was measured in digitonin-permeabilized cells as previously described (34). Chemiluminescence was determined as a function of time with Sirius L Tube luminometer (Titertek-Berthold, Pforzheim, Germany). The chemiluminescence signal was calibrated with an internal ATP standard after the addition of 10 μM oligomycin. The rates of the ATP synthesis were normalized to protein content and citrate synthase (CS) activity (35).

Evaluation of ROS levels

Quantification of H_2O_2 production was performed by flow cytometry. Briefly, cells were harvested, washed in PBS and aliquots of 5×10^5 cells were resuspended in Hank's Balanced Salt Solution 1X (Sigma-Aldrich, #H1387) containing 2 μM 2,7-dichlorodihydrofluorescein diacetate (H_2DCFDA, Life Technologies, #D399). Cells were incubated for 30 min at 37 °C protected from light. Flow cytometry analyses were performed in triplicate for each sample with a Coulter Epics XL-MCL (Beckman Coulter) equipped with an argon ion laser at $\lambda = 488$nm and $\lambda = 620$nm. Data were analyzed with WinMDI ver. 2.9 software (http://facs.scripps.edu/software.html; date last accessed March 2017).

Metabolomics

Metabolite concentrations were evaluated with Carcinoscope analysis (Human Metabolome Technologies, HMT) which uses capillary electrophoresis coupled to time of flight/triple quadrupole mass spectrometry and provides absolute quantification of 116 targeted metabolites. Metabolites were extracted using 100% methanol supplemented with 550 ul of Internal Standard Solution provided by HMT from 2 to 5 million cells seeded on 90mm plate. The metabolite concentrations were normalized to the number of viable cells.

2-DE isolation and protein identification by mass spectrometry (MS)

Cell pellets were resuspended in lysis buffer containing 7M urea, 2M thiourea, 4% CHAPS, protease inhibitor cocktail, 1mM sodium orthovanadate, 10 mM sodium fluoride and sonicated on ice for three rounds of 10", and processed as previously described (36). Briefly, protein samples (80 μg) were diluted up to 250 μl with rehydration buffer (lysis buffer, 65 mM DTT and 0.5% v/v IPG buffer) and applied to IPG strips (13 cm, pH 3-10 NL). Isoelectric focusing (IEF) and second dimension were performed with IPGphor IEF and Hoefer SE 600 Ruby electrophoresis (GE Healthcare). The IPG-strips were loaded and run on a 12% sodium dodecyl sulfate – polyacrylamide gel electrophoresis (SDS-PAGE) gel at constant current of 20mA/gel. Gels were fixed overnight in a fixing solution and stained. Gels were scanned by Image Master scanner at 300dpi and analyzed by Image Master software 5.0. The analysis was performed by comparing the volume% (vol%) of each spot, expressed as percentage of the spot volume over the total volume of all spots in the gel. Significant differences in protein levels were determined by Student's t-test. Differentially expressed proteins were identified by MS/MS. In detail, spots of interest were dehydrated with 50 μl acetonitrile for 10' and subjected to in-gel digestion as previously described (37). Peptides were analyzed by peptide mass fingerprinting (PMF) and MS/MS analysis with a MALDI-TOF/TOF Ultraflextreme, (Bruker Daltonics, #TN-31) in positive ion reflector mode (m/z range 500–4000), operating at 1kHz frequency and controlled by the FlexControl 3.4 software. External calibration was performed using the Peptide Standard Calibration II (Bruker Daltonics, #8222570). Spectra were processed using the software FlexAnalysis (version 3.4, Bruker Daltonics) and precursor ions with a signal to noise ratio greater than 10 selected for subsequent MS/MS analysis. MS data were exported by the software BioTools (version 3.2, Bruker Daltonics) and subjected to database search by using Matrix Science (www.matrixscience.com; date last accessed August 2016). Peptide masses were compared with those present in the SwissProt human protein database (release 2014_03 of 19-Mar-2014 of UniProtKB/TrEMBL, 54,247,468 sequence entries). The searching parameters were set as follows: peptide tolerance, 0.05Da; fragment mass tolerance, 0.25Da, enzyme, trypsin; missed cleavage, one; instrument, MALDI-TOF/TOF. Peptide tolerance was set to ±1.2Da, the MS/MS tolerance was set to 0.6Da, and searching peptide charge of 1+, 2+ and 3+ for ESI-Trap data. Protein dataset was subjected to KEGG pathway enrichment analysis using the software DAVID (david.abcc.ncifcrf.gov; date last accessed August 2016).

Western blot analysis

Whole proteins were extracted in RIPA buffer (Cell Signaling, #9806) and quantified by the Bradford protein assay (BIORAD, #5000006). Samples were separated by 12% SDS-PAGE and transferred to the Hybond ECL nitrocellulose membrane. After blocking, the membranes were probed by the appropriately diluted primary antibodies for 2 h at room temperature and subsequently, after opportune washes, were incubated with secondary antibody horseradish peroxidase-conjugated for 2 h at room temperature (1:2000 dilution). Immunoblots were developed using the ECL system.

The antibodies used were: mouse monoclonal anti-E-cadherin 1:1000 (Santa Cruz Biotechnology, #sc-71009) (38), mouse monoclonal anti-N-cadherin 1:1000 (Santa Cruz Biotechnology, #sc-59987) (38), mouse monoclonal anti-α-Tubulin 1:2000 (Santa Cruz Biotechnology, #sc-23948) (39), rabbit polyclonal anti-Ezrin (Santa Cruz Biotechnology, #sc-20773) (40), rabbit polyclonal pospho-Ezrin 1:1000 (Millipore, # 2040362) (41), rabbit polyclonal anti-Cofilin 1:1000 (Santa Cruz Biotechnology, #sc-33779) (42), rabbit polyclonal pospho -Cofilin (Ser3) 1:1000 (Santa Cruz Biotechnology, #sc-21867-R) (42), mouse monoclonal Anti-pospho-p44/42 MAPK (Erk 1/2) (thr202/tyr204) 1:2000 (Cell Signaling, #4370) (43) and rabbit polyclonal p44/42 MAPK (Erk1/2) 1:1000 (Cell Signaling, #4695) (43), mouse monoclonal anti- cyclin D1 1:200 (Santa Cruz Biotechnology #sc20044) (44), mouse monoclonal anti-vinculin 1:5000 (Sigma-Aldrich #V9131) (45). Secondary antibodies conjugated with HRP were from Invitrogen or Santa Cruz Biotechnology and used at 1:5000 dilution. Full blots with MW markers are available on request.

Wound healing assays

Cells were cultured to confluence in 6-well plates. Under aseptical conditions a thin wound was induced by scratching with a

200μl pipette tip and detached cells were rinsed with PBS. Using a phase contrast set up and a 10× magnification wound healing was continuously monitored by video camera to identify invading cells at different time points (12 h for OC cells and 8 h/24 h for cybrids). For quantitative evaluation, 20 sequential open wound areas were analyzed with T-scratch software (CSElab) and the capacity to invade was expressed as the percentage of open wound area.

Immunofluorescence microscopy

Scratch of confluent monolayer of cells seeded on 11-mm round glass coverslips was performed for wound-healing assays. After 6 h of incubation at 37 °C under 5% CO_2 cells were fixed in 3% paraformaldehyde, permeabilized with piperazine-N,N′-bis (2-ethanesulfonic acid) (PIPES), Saponin 0.1%, and incubated with primary antibodies for 20'. After 3 washes with PBS-Saponin 0.1%, cells were incubated for 20' with secondary antibodies and then with the DAPI dye (1 μg/ml). The antibodies used were: rabbit polyclonal anti-giantin 1:1000 (Abcam, #Ab24586) (46), mouse monoclonal anti-tubulin 1:2000 (Sigma-Aldrich, #T5168) (47), anti-rabbit AlexaFluor488 1:500 (Invitrogen, #A-11034). Actin staining was performed with Actin-Stain 555 phalloidin (PHDH1, Cytoskeleton) (48). Subsequently, cells were imaged by using a confocal microscope Zeiss LSM 700 (Germany). DAPI was excited with the 405nm laser diode and emission was collected from 415nm to 500nm. Anti-rabbit AlexFluor488 was excited with a 488nm argon laser and emission was collected from 510nm to 550nm. TRITC of Actin-Stain 555 was excited with a helium-neon laser for excitation at 555nm and emission was collected from 560 to 615nm. Images were taken with a Plan - Apochromat 63×/1.40na oil-immersion objective and a pinhole aperture of 1 Airyunit. Cells with Golgi structures located in the upper/lower third of the cell facing the wound were considered as polarized. The orientation of the Golgi was evaluated on 100 cells for cybrids and 50 cells for OC models.

Statistics

The evaluation of statistical significance was defined using a two-tailed Student's *t*-test unless otherwise indicated.

Supplementary Material

Supplementary Material is available at *HMG* online.

Acknowledgements

We thank the Pierfranco and Luisa Mariani Foundation. A.M. Porcelli and C. Bucci were supported by Associazione Italiana Ricerca sul Cancro (AIRC). G. Gasparre was supported by EU FP7 Marie Curie project MEET-317433. G. Girolimetti was supported by a triennial AIRC fellowship "Livia Perotti". F. Guerra was supported by Regione Puglia grant T7WGSJ3 "Sviluppo di nuove metodologie e strumenti Innovativi per la diagnoSI ed il trattamento Terapeutico di tumori Epiteliali uMAni (SISTEMA)". We also thank 2HE-PONa3_00334 project for the Zeiss LSM700 confocal microscope. We are grateful to Dr. Giovanna Farruggia and Dr. Manuela Voltattorni for technical assistance for flow cytometry experiments.

Conflict of Interest statement. None declared.

Funding

Associazione Italiana Ricerca sul Cancro (AIRC) – grant IG17387 and IG19068, AIRC grant IG14242, the Italian ministry of Health – grant DISCO TRIP #GR-2013-02356666, and EU FP7 Marie Curie project MEET-317433, triennial AIRC fellowship "Livia Perotti", Regione Puglia grant T7WGSJ3 "Sviluppo di nuove metodologie e strumenti Innovativi per la diagnoSI ed il trattamento Terapeutico di tumori Epiteliali uMAni (SISTEMA)".

References

1. Belani, C.P., Chakraborty, B., Modi, R. and Khamar, B. (2016) A randomized trial of TLR-2 agonist CADI-05 targeting desmocollin-3 for advanced non-small-cell lung cancer. *Ann. Oncol.*, **28**, 298–304. 10.1093/annonc/mdw608.
2. Abdo, J., Agrawal, D.K. and Mittal, S.K. (2017) Basis for molecular diagnostics and immunotherapy for esophageal cancer. *Expert Rev. Anticancer Ther.*, **17**, 33–45.
3. Coleman, R.L., Monk, B.J., Sood, A.K. and Herzog, T.J. (2013) Latest research and treatment of advanced-stage epithelial ovarian cancer. *Nat. Rev. Clin. Oncol.*, **10**, 211–224.
4. Cheung-Ong, K., Giaever, G. and Nislow, C. (2013) DNA-damaging agents in cancer chemotherapy: serendipity and chemical biology. *Chem. Biol.*, **20**, 648–659.
5. Talarico, T., Cullinane, C.M., Gray, P.J., Webster, L.K., Deacon, G.B. and Phillips, D.R. (2001) Nuclear and mitochondrial distribution of organoamidoplatinum(II) lesions in cisplatin-sensitive and -resistant adenocarcinoma cells. *Anticancer. Drug Des.*, **16**, 135–141.
6. Mullen, A.R., Wheaton, W.W., Jin, E.S., Chen, P.-H., Sullivan, L.B., Cheng, T., Yang, Y., Linehan, W.M., Chandel, N.S. and DeBerardinis, R.J. (2012) Reductive carboxylation supports growth in tumour cells with defective mitochondria. *Nature*, **481**, 385–388.
7. He, Y., Wu, J., Dressman, D.C., Iacobuzio-Donahue, C., Markowitz, S.D., Velculescu, V.E., Diaz, L.A.J., Kinzler, K.W., Vogelstein, B. and Papadopoulos, N. (2010) Heteroplasmic mitochondrial DNA mutations in normal and tumour cells. *Nature*, **464**, 610–614.
8. Iommarini, L., Kurelac, I., Capristo, M., Calvaruso, M.A., Giorgio, V., Bergamini, C., Ghelli, A., Nanni, P., De Giovanni, C., Carelli, V. *et al.* (2014) Different mtDNA mutations modify tumor progression in dependence of the degree of respiratory complex I impairment. *Hum. Mol. Genet.*, **23**, 1453–1466.
9. Smolkova, K., Plecita-Hlavata, L., Bellance, N., Benard, G., Rossignol, R. and Jezek, P. (2011) Waves of gene regulation suppress and then restore oxidative phosphorylation in cancer cells. *Int. J. Biochem. Cell Biol.*, **43**, 950–968.
10. Tallini, G. (1998) Oncocytic tumours. *Virchows Arch. Int. J. Pathol.*, **433**, 5–12.
11. Gasparre, G., Kurelac, I., Capristo, M., Iommarini, L., Ghelli, A., Ceccarelli, C., Nicoletti, G., Nanni, P., De Giovanni, C., Scotlandi, K. *et al.* (2011) A mutation threshold distinguishes the antitumorigenic effects of the mitochondrial gene MTND1, an oncojanus function. *Cancer Res.*, **71**, 6220–6229.
12. Guerra, F., Perrone, A.M., Kurelac, I., Santini, D., Ceccarelli, C., Cricca, M., Zamagni, C., De Iaco, P. and Gasparre, G. (2012) Mitochondrial DNA mutation in serous ovarian cancer: implications for mitochondria-coded genes in chemoresistance. *J. Clin. Oncol.*, **30**, e373–e378.
13. Moro, L., Arbini, A.A., Marra, E. and Greco, M. (2008) Mitochondrial DNA depletion reduces PARP-1 levels and

promotes progression of the neoplastic phenotype in prostate carcinoma. *Cell. Oncol.*, **30**, 307–322.
14. Catanzaro, D., Gaude, E., Orso, G., Giordano, C., Guzzo, G., Rasola, A., Ragazzi, E., Caparrotta, L., Frezza, C. and Montopoli, M. (2015) Inhibition of glucose-6-phosphate dehydrogenase sensitizes cisplatin-resistant cells to death. *Oncotarget*, **6**, 30102–30114.
15. Ishikawa, K., Takenaga, K., Akimoto, M., Koshikawa, N., Yamaguchi, A., Imanishi, H., Nakada, K., Honma, Y. and Hayashi, J.-I. (2008) ROS-generating mitochondrial DNA mutations can regulate tumor cell metastasis. *Science*, **320**, 661–664.
16. Olson, M.F. and Sahai, E. (2009) The actin cytoskeleton in cancer cell motility. *Clin. Exp. Metastasis*, **26**, 273–287.
17. Pacheco, A. and Gallo, G. (2016) Actin filament-microtubule interactions in axon initiation and branching. *Brain Res. Bull.*, **126**, 300–310. 10.1016/j.brainresbull.2016.07.013.
18. Sainath, R., Ketschek, A., Grandi, L. and Gallo, G. (2016) CSPGs inhibit axon branching by impairing mitochondria-dependent regulation of actin dynamics and axonal translation. *Dev. Neurobiol.*, **77**, 454–473. 10.1002/dneu.22420.
19. Nishitani, S., Noma, K., Ohara, T., Tomono, Y., Watanabe, S., Tazawa, H., Shirakawa, Y. and Fujiwara, T. (2016) Iron depletion-induced downregulation of N-cadherin expression inhibits invasive malignant phenotypes in human esophageal cancer. *Int. J. Oncol.*, **49**,1351–1359 10.3892/ijo.2016.3640.
20. Rodriguez, F.J., Lewis-Tuffin, L.J. and Anastasiadis, P.Z. (2012) E-cadherin's dark side: possible role in tumor progression. *Biochim. Biophys. Acta*, **1826**, 23–31.
21. Jayson, G.C., Kohn, E.C., Kitchener, H.C. and Ledermann, J.A. (2014) Ovarian cancer. *Lancet Lond. Engl.*, **384**, 1376–1388.
22. Shi, H., Pan, L. and Song, T. (2009) Impact of platinum on the whole mitochondrial genome of ovarian carcinomas both in vivo and in vitro. *Int. J. Gynecol. Cancer*, **19**, 423–430.
23. Mizutani, S., Miyato, Y., Shidara, Y., Asoh, S., Tokunaga, A., Tajiri, T. and Ohta, S. (2009) Mutations in the mitochondrial genome confer resistance of cancer cells to anticancer drugs. *Cancer Sci.*, **100**, 1680–1687.
24. Zong, W.-X., Rabinowitz, J.D. and White, E. (2016) Mitochondria and Cancer. *Mol. Cell*, **61**, 667–676.
25. Sansone, P., Ceccarelli, C., Berishaj, M., Chang, Q., Rajasekhar, V.K., Perna, F., Bowman, R.L., Vidone, M., Daly, L., Nnoli, J. *et al.* (2016) Self-renewal of CD133(hi) cells by IL6/Notch3 signalling regulates endocrine resistance in metastatic breast cancer. *Nat. Commun.*, **7**, 10442.
26. Haq, R., Shoag, J., Andreu-Perez, P., Yokoyama, S., Edelman, H., Rowe, G.C., Frederick, D.T., Hurley, A.D., Nellore, A., Kung, A.L. *et al.* (2013) Oncogenic BRAF regulates oxidative metabolism via PGC1alpha and MITF. *Cancer Cell*, **23**, 302–315.
27. Mariotti, C., Tiranti, V., Carrara, F., Dallapiccola, B., DiDonato, S. and Zeviani, M. (1994) Defective respiratory capacity and mitochondrial protein synthesis in transformant cybrids harboring the tRNA(Leu(UUR)) mutation associated with maternally inherited myopathy and cardiomyopathy. *J. Clin. Invest.*, **93**, 1102–1107.
28. Kurelac, I., MacKay, A., Lambros, M.B.K., Di Cesare, E., Cenacchi, G., Ceccarelli, C., Morra, I., Melcarne, A., Morandi, L., Calabrese, F.M. *et al.* (2013) Somatic complex I disruptive mitochondrial DNA mutations are modifiers of tumorigenesis that correlate with low genomic instability in pituitary adenomas. *Hum. Mol. Genet.*, **22**, 226–238.
29. Calabrese, C., Simone, D., Diroma, M.A., Santorsola, M., Gutta, C., Gasparre, G., Picardi, E., Pesole, G. and Attimonelli, M. (2014) MToolBox: a highly automated pipeline for heteroplasmy annotation and prioritization analysis of human mitochondrial variants in high-throughput sequencing. *Bioinforma. Oxf. Engl.*, **30**, 3115–3117.
30. Santorsola, M., Calabrese, C., Girolimetti, G., Diroma, M.A., Gasparre, G. and Attimonelli, M. (2016) A multi-parametric workflow for the prioritization of mitochondrial DNA variants of clinical interest. *Hum. Genet.*, **135**, 121–136.
31. Rubino, F., Piredda, R., Calabrese, F.M., Simone, D., Lang, M., Calabrese, C., Petruzzella, V., Tommaseo-Ponzetta, M., Gasparre, G. and Attimonelli, M. (2012) HmtDB, a genomic resource for mitochondrion-based human variability studies. *Nucleic Acids Res.*, **40**, D1150–D1159.
32. Kurelac, I., Lang, M., Zuntini, R., Calabrese, C., Simone, D., Vicario, S., Santamaria, M., Attimonelli, M., Romeo, G. and Gasparre, G. (2012) Searching for a needle in the haystack: comparing six methods to evaluate heteroplasmy in difficult sequence context. *Biotechnol. Adv.*, **30**, 363–371.
33. Iommarini, L., Calvaruso, M.A., Kurelac, I., Gasparre, G. and Porcelli, A.M. (2013) Complex I impairment in mitochondrial diseases and cancer: parallel roads leading to different outcomes. *Int. J. Biochem. Cell Biol.*, **45**, 47–63.
34. Ghelli, A., Tropeano, C.V., Calvaruso, M.A., Marchesini, A., Iommarini, L., Porcelli, A.M., Zanna, C., De Nardo, V., Martinuzzi, A., Wibrand, F. *et al.* (2013) The cytochrome b p.278Y>C mutation causative of a multisystem disorder enhances superoxide production and alters supramolecular interactions of respiratory chain complexes. *Hum. Mol. Genet.*, **22**, 2141–2151.
35. Trounce, I.A., Kim, Y.L., Jun, A.S. and Wallace, D.C. (1996) Assessment of mitochondrial oxidative phosphorylation in patient muscle biopsies, lymphoblasts, and transmitochondrial cell lines. *Methods Enzymol.*, **264**, 484–509.
36. Vergara, D., Simeone, P., Toraldo, D., Del Boccio, P., Vergaro, V., Leporatti, S., Pieragostino, D., Tinelli, A., De Domenico, S., Alberti, S. *et al.* (2012) Resveratrol downregulates Akt/GSK and ERK signalling pathways in OVCAR-3 ovarian cancer cells. *Mol. Biosyst.*, **8**, 1078–1087.
37. Vergara, D., Chiriaco, F., Acierno, R. and Maffia, M. (2008) Proteomic map of peripheral blood mononuclear cells. *Proteomics*, **8**, 2045–2051.
38. Vergara, D., Ferraro, M.M., Cascione, M., Del Mercato, L.L., Leporatti, S., Ferretta, A., Tanzarella, P., Pacelli, C., Santino, A., Maffia, M. *et al.* (2015) Cytoskeletal alterations and biomechanical properties of parkin-mutant human primary fibroblasts. *Cell Biochem. Biophys.*, **71**, 1395–1404.
39. Cremonini, E., Bettaieb, A., Haj, F.G., Fraga, C.G. and Oteiza, P.I. (2016) (-)-Epicatechin improves insulin sensitivity in high fat diet-fed mice. *Arch. Biochem. Biophys.*, **599**, 13–21.
40. Nüesch, J.P.F., Bär, S., Lachmann, S. and Rommelaere, J. (2009) Ezrin-radixin-moesin family proteins are involved in parvovirus replication and spreading. *J. Virol.*, **83**, 5854–5863.
41. Sullivan, S., Pells, S., Hooper, M., Gallagher, E. and McWhir, J. (2006) Nuclear reprogramming of somatic cells by embryonic stem cells is affected by cell cycle stage. *Cloning Stem Cells*, **8**, 174–188.
42. Vergara, D., Valente, C.M., Tinelli, A., Siciliano, C., Lorusso, V., Acierno, R., Giovinazzo, G., Santino, A., Storelli, C. and Maffia, M. (2011) Resveratrol inhibits the epidermal growth factor-induced epithelial mesenchymal transition in MCF-7 cells. *Cancer Lett.*, **310**, 1–8.
43. Winship, A.L., Rainczuk, K., Ton, A. and Dimitriadis, E. (2016) Fibulin-5 localisation in human endometrial cancer shifts from epithelial to stromal with increasing tumour grade,

and silencing promotes endometrial epithelial cancer cell proliferation. *Oncol. Lett.*, **12**, 651–657.
44. Tiwari, P., Sahay, S., Pandey, M., Qadri, S.S.Y.H. and Gupta, K.P. (2016) Preventive effects of butyric acid, nicotinamide, calcium glucarate alone or in combination during the 7, 12-dimethylbenz (a) anthracene induced mouse skin tumorigenesis via modulation of K-Ras-PI3K-AKTpathway and associated micro RNAs. *Biochimie*, **121**, 112–122.
45. Liu, M., Sakamaki, T., Casimiro, M.C., Willmarth, N.E., Quong, A.A., Ju, X., Ojeifo, J., Jiao, X., Yeow, W.-S., Katiyar, S. *et al.* (2010) The canonical NF-kappaB pathway governs mammary tumorigenesis in transgenic mice and tumor stem cell expansion. *Cancer Res.*, **70**, 10464–10473.
46. Chaumet, A., Wright, G.D., Seet, S.H., Tham, K.M., Gounko, N.V. and Bard, F. (2015) Nuclear envelope-associated endosomes deliver surface proteins to the nucleus. *Nat. Commun.*, **6**, 8218.
47. Jiwani, S., Wang, Y., Dowd, G.C., Gianfelice, A., Pichestapong, P., Gavicherla, B., Vanbennekom, N. and Ireton, K. (2012) Identification of components of the host type IA phosphoinositide 3-kinase pathway that promote internalization of Listeria monocytogenes. *Infect. Immun.*, **80**, 1252–1266.
48. Burks, J., Reed, R.E. and Desai, S.D. (2014) ISGylation governs the oncogenic function of Ki-Ras in breast cancer. *Oncogene*, **33**, 794–803.